Aalto University

OPEN ACCESS

This is an electronic reprint of the original article.
This reprint may differ from the original in pagination and typographic detail.

Meng, Lingju; Akhoundian, Maedeh; Al Azawi, Anas; Shoja, Yalda; Chi, Pei-Yin; Meinander, Kristoffer; Suihkonen, Sami; Franssila, Sami

Ultrasensitive Monolithic Dopamine Microsensors Employing Vertically Aligned Carbon Nanofibers

Published in:
Advanced Healthcare Materials

DOI:
10.1002/adhm.202303872

Published: 17/07/2024

Document Version
Publisher's PDF, also known as Version of record

Published under the following license:
CC BY

Please cite the original version:
Meng, L., Akhoundian, M., Al Azawi, A., Shoja, Y., Chi, P.-Y., Meinander, K., Suihkonen, S., & Franssila, S. (2024). Ultrasensitive Monolithic Dopamine Microsensors Employing Vertically Aligned Carbon Nanofibers. *Advanced Healthcare Materials* , *13*(18), Article 2303872. https://doi.org/10.1002/adhm.202303872

This material is protected by copyright and other intellectual property rights, and duplication or sale of all or part of any of the repository collections is not permitted, except that material may be duplicated by you for your research use or educational purposes in electronic or print form. You must obtain permission for any other use. Electronic or print copies may not be offered, whether for sale or otherwise to anyone who is not an authorised user.

Check for updates

ADVANCED HEALTHCARE MATERIALS
www.advhealthmat.de

Ultrasensitive Monolithic Dopamine Microsensors Employing Vertically Aligned Carbon Nanofibers

Lingju Meng, Maedeh Akhoundian, Anas Al Azawi, Yalda Shoja, Pei-Yin Chi, Kristoffer Meinander, Sami Suihkonen, and Sami Franssila**

Brain-on-Chip devices, which facilitate on-chip cultures of neurons to simulate brain functions, are receiving tremendous attention from both fundamental and clinical research. Consequently, microsensors are being developed to accomplish real-time monitoring of neurotransmitters, which are the benchmarks for neuron network operation. Among these, electrochemical sensors have emerged as promising candidates for detecting a critical neurotransmitter, dopamine. However, current state-of-the-art electrochemical dopamine sensors are suffering from issues like limited sensitivity and cumbersome fabrication. Here, a novel route in monolithically microfabricating vertically aligned carbon nanofiber electrochemical dopamine microsensors is reported with an anti-blistering slow cooling process. Thanks to the microfabrication process, microsensors is created with complete insulation and large surface areas. The champion device shows extremely high sensitivity of 4.52× 10^4 μAμM^{-1}·cm^{-2}, which is two-orders-of-magnitude higher than current devices, and a highly competitive limit of detection of 0.243 nM. These remarkable figures-of-merit will open new windows for applications such as electrochemical recording from a single neuron.

1. Introduction

The brain is the most complex organ in our bodies and probably more complicated than the known universe.[1] It contains 86 billion neurons and 60 trillion connections, which makes it challenging to study, let alone understand how it is related to consciousness[2] and neurodegenerative diseases such as Alzheimer's and Parkinson's diseases.[3,4] Neurodegenerative diseases affect nearly one billion people worldwide, according to the World Health Organization (WHO).[4] Thus, generations of scientists have been trying to demystify the human brain via different routes, from in vivo investigation[5–7] to numerical brain simulation.[8] During the past two decades, because of the boom in semiconductor manufacturing techniques and microfluidics,[9] the Brain-on-a-Chip (BoC) technology, which builds microfluidic chips to simulate the function of the brain, has achieved tremendous development.[4,10–12] To simulate different functions in a brain, various BoC devices have been developed (e.g., neural circuits[13], blood-brain barrier[14,15]). BoC can not only be utilized in fundamental research[14,16] but also provide a fast, cost-effective route in drug screening in the pharmaceutical industry because of its ability to be mass-produced by microfabrication technologies and ease in using.[17]

Biosensing technology is in rapid development for monitoring various cell activities (electrical, mechanical, electrophysiological, electromechanical, electrochemical, etc.) on BoC devices.[18–23] Among them, electrochemical biosensors stand out because of their capability of fast, real-time monitoring the neurotransmitters (NTs). NTs are the signalling molecules that

L. Meng, A. Al Azawi, Y. Shoja, P.-Y. Chi, S. Franssila
Department of Chemistry and Materials Science
Aalto University
Espoo 02150, Finland
E-mail: lingju.meng@aalto.fi; sami.franssila@aalto.fi
L. Meng, A. Al Azawi, Y. Shoja, P.-Y. Chi, S. Franssila
Micronova Nanofabrication Centre
Aalto University
Espoo 02150, Finland
M. Akhoundian
Department of Electrical Engineering and Automation
Aalto University
Espoo 02150, Finland
K. Meinander
Department of Bioproducts and Biosystems
Aalto University
Espoo 02150, Finland
S. Suihkonen
Department of Electronics and Nanoengineering
Aalto University
Espoo 02150, Finland
The ORCID identification number(s) for the author(s) of this article can be found under https://doi.org/10.1002/adhm.202303872

© 2024 The Author(s). Advanced Healthcare Materials published by Wiley-VCH GmbH. This is an open access article under the terms of the Creative Commons Attribution License, which permits use, distribution and reproduction in any medium, provided the original work is properly cited.

DOI: 10.1002/adhm.202303872

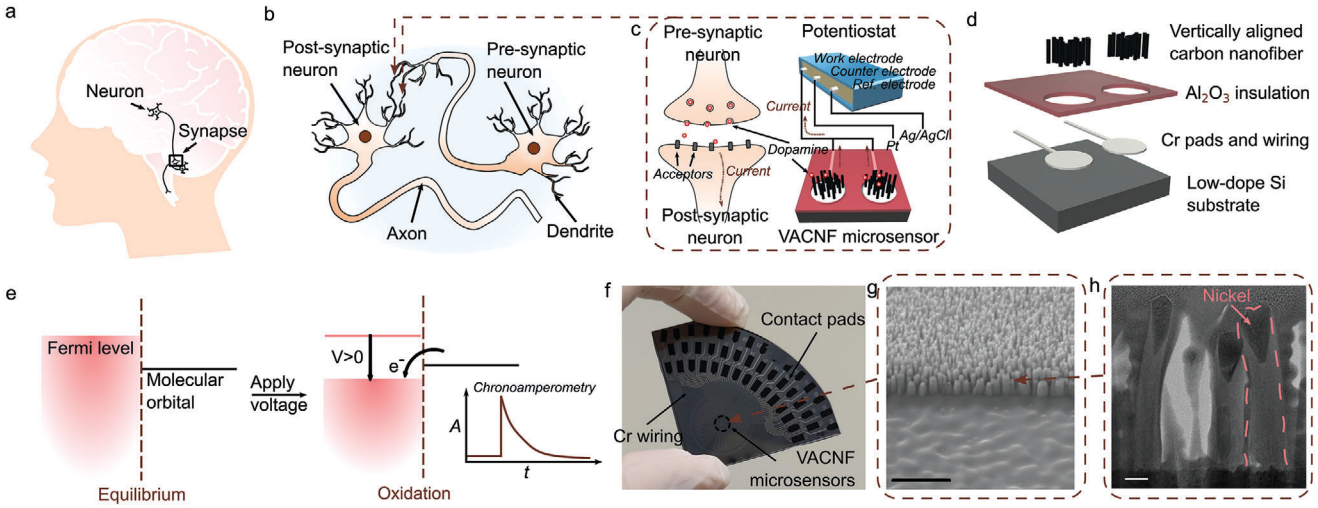

Figure 1. Illustration of the device setup, structure, and working mechanism: a) Illustration of the neurons and synapses in the human brain. b) Illustration of a pre-synaptic neuron and a post-synaptic neuron. c) How dopamine as a neurotransmitter is transmitted in a synapse, and how does the microsensor detect dopamine. d) Exploded view of the microsensor structure. e) The working mechanism of the electrochemical microsensor. f) Photo of the microfabricated microsensors. g) SEM image of the carbon nanofibers. The scale bar indicates 100 nm. h) TEM micrograph of the carbon nanofibers. The scale bar indicates 100 nm.

carry signals from one neuron to another across a synapse, as shown in **Figure** 1a–c. Abnormal concentrations and dysfunction of NTs are considered indicators of neurodegenerative diseases.[24,25] Dopamine (3,4-dihydroxyphenethylamine), as a critical NT, posits significant roles in multiple physiological processes, and abnormal dopamine concentrations can be related to several neurological disorders, such as the aforementioned Alzheimer's and Parkinson's diseases.[26] Consequently, there has been a significant drive to develop suitable biosensors for dopamine (DA) detection in recent years. Proper biosensors for DA detection should possess high selectivity, high sensitivity and biocompatibility. Additionally, considering the BoC applications, the detection should be fast and cost-effective. Traditional DA detection strategies are enzyme-linked immunosorbent assay (ELISA) and high-performance liquid chromatography (HPLC) associated with various electrical, optical, or mass spectroscopy methods.[27–29] However, these strategies involve costly equipment and require rigorous sample preparation,[26,30,31] which make them incompatible with BoC applications. Photonic biosensors have also been investigated in recent years to reduce the device cost and improve data acquisition speed. This class of sensors relies on the shift of localized surface plasmon resonance and surface plasmon polariton resonance.[31–33] However, this route requires an additional light source and suffers from data processing complexity (full spectrum scan and peak position search). Electrochemical sensors[34–36] are the most promising candidate for on-chip DA detection because of fast, real-time monitoring of the NTs and ease of use. However, current electrochemical biosensors have limited selectivity (interference from ascorbic acid, etc.) and low sensitivity (from under one to hundreds of $\mu A \mu M^{-1} \cdot cm^{-2}$), along with the severe biofouling (electro-polymerization rendering the device inactive).[37,38]

In recent years, vertically aligned carbon nanofibers (VACNFs) have come to the spotlight of biosensing. VACNFs consist of carbon nanofibers oriented with their longitudinal axis perpendicular to a substrate surface. On one hand, carbon materials hold superior biocompatibility to most neural cells. Moreover, unlike planar carbon electrodes like diamond-like carbon electrodes, the rough surface of VACNF electrodes will significantly reduce bio-fouling[39] and increase the surface area to enhance the sensitivity.[39,40] VACNF electrodes also contain the capability of high-selectivity sensing, which is highly appreciated in DA detection to distinguish DA from ascorbic acid (AA) and other interference molecules.[41,42] Several electrochemical biosensors utilizing VACNFs have been reported.[43–48] However, to accomplish monolithic microsensors compatible with BoC devices, there are still obstacles regarding device fabrication. The key problem is that due to the high temperature in VACNF growth (CVD process with temperature over 600°C), blistering defects will occur on the prepared insulation layer before this step, and the insulation is an essential part of the device because it will reduce the signal noise level. Multiple compromised routes have been developed to avoid this problem (summarized in Table S1, Supporting Information): 1) Some researchers chose to pattern the insulation after the growth of VACNFs.[49] Because of the forest-like morphology of the VACNFs, multiple solvent procedures in photolithography will damage the VACNFs by the large surface tension during evaporation. So this method can only be applied to single or sparse carbon nanofibers, which are unsuitable for high-sensitivity biosensing. 2) Encapsulation (embedding nanofibers into a matrix material) is another popular route to solve the problem.[43,45] However, the matrix material will make the VACNFs lose their large surface areas, the desired property for high-sensitivity electrochemical sensing. 3) Handmade devices can always avoid the aforementioned problems, but their cumbersome fabrication process is unsuitable for BoC devices and future monolithic mass manufacturing. Thus, a fabrication process for a monolithic VACNF microsensor is the need of hour.

© 2024 The Author(s). Advanced Healthcare Materials published by Wiley-VCH GmbH

21922659, 2024, 18, Downloaded from https://onlinelibrary.wiley.com/doi/10.1002/adhm.202303872 by Aalto University, Wiley Online Library on [21/07/2024]. See the Terms and Conditions (https://onlinelibrary.wiley.com/terms-and-conditions) on Wiley Online Library for rules of use; OA articles are governed by the applicable Creative Commons License

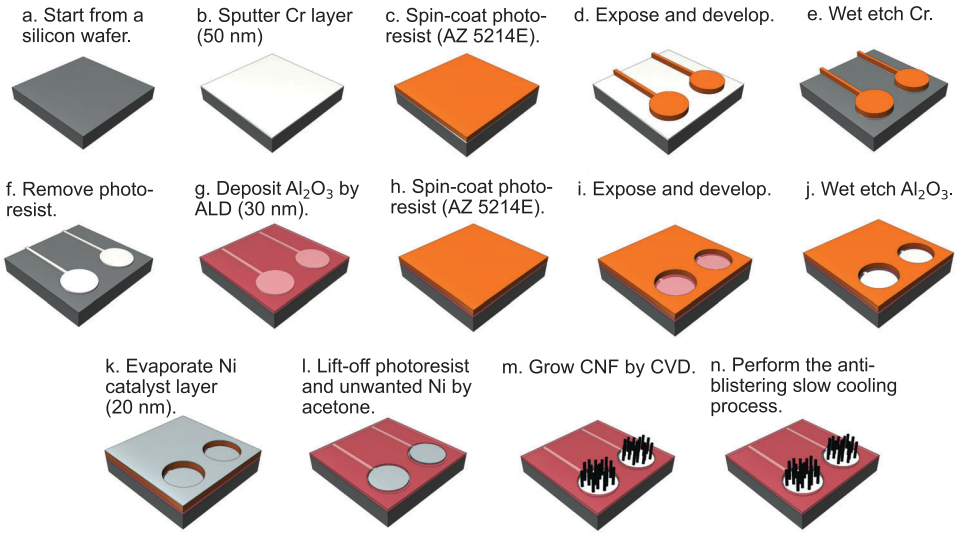

Figure 2. Microfabrication process flow of the VACNF microsensors.

Here, a novel process that avoids blistering sites on the insulation layer was reported by us. This process enables the microfabrication of monolithic VACNF microsensors. Cyclic voltammetry and chronoamperometry were utilized to characterize our VACNF microsensor. In the chronoamperometry measurement, tiny amounts of pipette injection of DA (dosage varying from 0.2 pmol to 10 pmol, concentration varying from 25 nM to 1 µM) in an environment of organoid media are exploited to evaluate the microsensor's ability for in vitro neuron recording. In our tests, our VACNF microsensor powered by the novel process shows record-high sensitivity of 4.52×10^4 $\mu A \mu M^{-1} \cdot cm^{-2}$, which is two-order-of-magnitude higher than current state-of-the-art devices.[48,50,51] The limit of detection (0.243 nM) of our VACNF microsensor is also among the lowest. The outstanding performance of our microsensor will open new windows for currently challenging but demanding applications for BoC chips, e.g., electrochemical recording of a single neuron.

2. Results

2.1. Device Structure and Working Principle

The VACNF microsensor consists of four parts: the Si substrate, Cr wirings and pads, the Al_2O_3 insulation layer, and VACNF electrodes (Figure 1d). The working mechanism of the electrochemical DA sensor is based on the redox reaction on the interface of the VACNF electrode, as shown in Figure 1e. In an equilibrium state without external potential, the Fermi level of the VACNFs is higher than the highest occupied molecular orbital (HOMO) of an adjacent DA molecule. Initially, dopamine molecules adsorb onto the surface of the CNF electrode through various interactions, such as non-covalent π-π stacking, hydrogen bonding, and electrostatic interactions, facilitating subsequent reactions. When the external potential is applied to the electrode, its Fermi level will be lowered below the HOMO of the DA molecule. Thus, electrons on the DA molecule's HOMO will be transferred to the electrode. An oxidation reaction will occur, and an electrical current will be generated. This oxidation current will be the characteristic signal of our VACNF microsensor. During the reaction, dopamine molecules will be transitioning between different redox states: dopamine (DA), dopamine semiquinone radical, and dopamine quinone (DAQ). DAQ is the primary oxidation product, formed by removing two electrons and two protons. This process releases protons and water molecules as byproducts. Various oxidation products like dopaminechrome and dopamine ortho-quinone may also form during the process.[41] The final produced device was with electrodes consisting of free-standing, vertically aligned carbon nanofibers as shown in the optical image (Figure 1f), scanning electron microscope (SEM) image (Figure 1g) and transmission electron microscope (TEM) image (Figure 1h).

2.2. Device Fabrication

Microsensors were fabricated in a two-layer photolithography process (**Figure 2**). The Cr layer were first deposited on a Si wafer by sputtering (step (a) and (b)). Then the photoresist AZ 5214E layer was pattern on the Cr by a standard spin-coating (step (c)), exposing, and developing (step (d)) photolithography process. The photoresist patterns was then used as the etching mask to wet-etch the Cr to create the Cr patterns (step (e)). After the photoresist was removed, a 30 nm of Al_2O_3 layer was deposited onto the wafer by ALD (step (g)). The second photolithography process (step (h) and (i)) was similar as the first one, after which the etch mask for Al_2O_3 etching will be generated to define the electrode area. Subsequently, the Al_2O_3 covering the electrode area was wet-etched (step (j)). After that, the Ni catalyst layer was patterned via the lift-off route by evaporation (step (k)) and acetone ultrasonication bath (step (l)), and the VACNFs were grown on the patterned Ni afterward (step (m)). At last, our unique anti-blistering process was applied after the VACNF growth, as shown in step (n), resulting in uniform surfaces with minimal blisters. Details of the fabrication process are shown in the Experimental Section with references to the Supporting Information.

© 2024 The Author(s). Advanced Healthcare Materials published by Wiley-VCH GmbH

21922659, 2024, 18, Downloaded from https://onlinelibrary.wiley.com/doi/10.1002/adhm.202303872 by Aalto University, Wiley Online Library on [21/07/2024]. See the Terms and Conditions (https://onlinelibrary.wiley.com/terms-and-conditions) on Wiley Online Library for rules of use; OA articles are governed by the applicable Creative Commons License

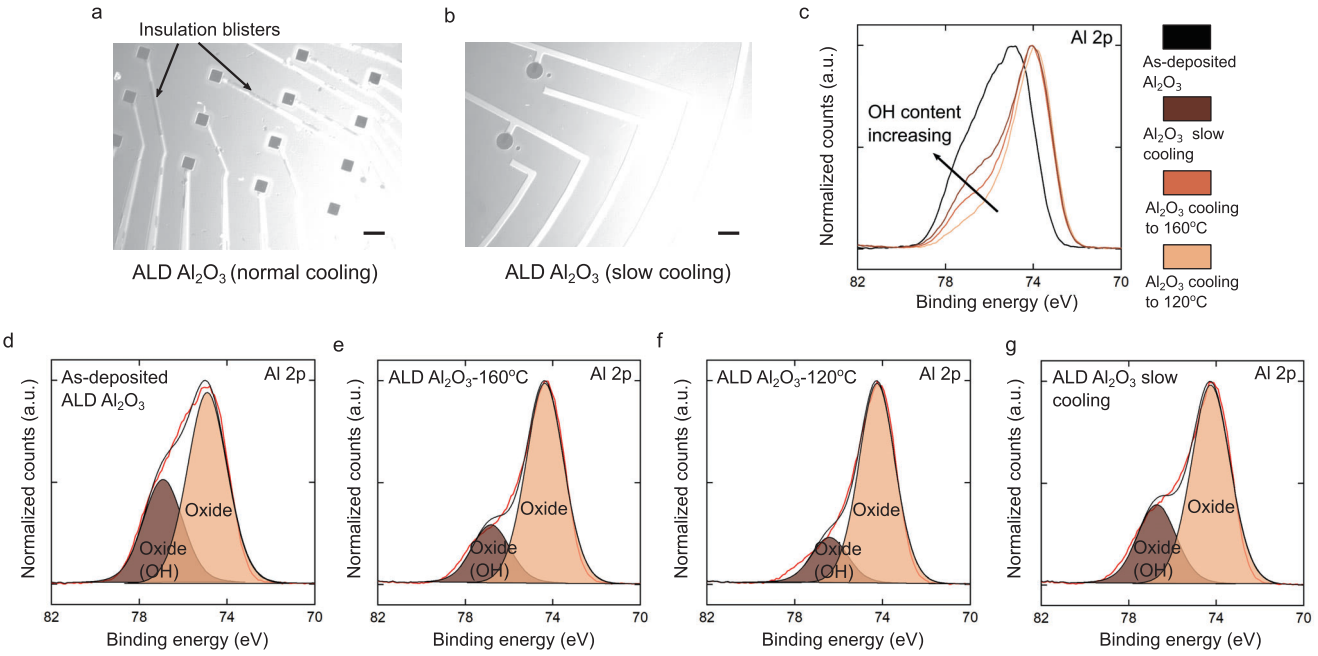

Figure 3. Analysis of the blisters on the alumina thin films: a) Al_2O_3 film peeling off shown on the device after 600°C growth of VACNFs then finally cooling to 120°C in the reaction chamber, and transferred to the ambient environment for fast cooling. The scale bar is 200 µm. b) Al_2O_3 film shown on the device after high-temperature growth of VACNFs then cooling down slowly in the reaction chamber to room temperature. The scale bar is 200 µm. c) Comparison of Al 2p XPS spectra from Al_2O_3 films with different cooling approaches. d–g) Al 2p XPS spectra fittings of Al_2O_3 films with different cooling approaches.

2.3. VACNF Characterization

From the cross-section created by the focused ion beam, it can be verified from the SEM image (Figure 1g) that the CNFs are evenly vertically aligned. As an essential analytical method for carbon materials, the Raman spectrum (Figure S1, Supporting Information) was acquired to retrieve more information on the VACNFs. The broad D band at 1360 cm^{-1} indicates the fiber structure, while the 2D resonance peak at ≈2800 cm^{-1} shows the crystalline nature of the VACNFs.[42,52,53] X-ray photoelectron spectroscopy (XPS) was performed to investigate the composition of the VACNF surfaces. The spectra are shown in Figure S2 (Supporting Information). The survey spectrum (Figure S2a, Supporting Information) shows that except for the carbon peaks and oxygen peaks, there are also Ni peaks from the catalyst and Cr peaks from the growth bed (Cr wirings). A deconvolution of the C 1s spectrum in Figure S2b (Supporting Information) shows that ≈45% of the carbon components of the sample are graphite, which coincides with the Raman spectrum. Figures S2c–S2f (Supporting Information) show the O 1s and Ni 2p peak sets. Details are described in the Supporting Information. It should be noted that the deconvolution of the Ni 2p in accordance with Biesinger et al.[54] shows that the majority of Ni is in a metallic state (>80%).

2.4. Analysis of the Blisters on the Alumina Thin Films

As stated in the introduction section, the high temperature (≈600°C) in the VACNF growth will cause blisters on the Al_2O_3 thin film because of the thermal expansion and gassing process.[55,56] It has still been a problem haunting the researchers willing to develop microsensors based on VACNFs.

During our device fabrication process, in order to avoid blisters, a new cooling process, the anti-blistering slow cooling process, was developed. In a normal cooling process after the VACNF growth, as the chamber temperature reaches between 200 to 100°C, the samples will be removed from the chamber for final cooling in the ambient environment. In our slow cooling process, the samples will remain in the reaction chamber till room temperature, which takes roughly four hours. Details of these two cooling strategies can be found in the illustration in Figure S3 (Supporting Information). A sample temperature monitoring curve of the first stage of the cooling process is shown in Figure S4 (Supporting Information). The cooling rate of the critical second stage (after Ar flow stopped as shown in Figure S3, Supporting Information) of the slow cooling process can be estimated as 0.72°Cmin^{-1}. An optical microscope image (**Figure 3a**) shows that by a normal cooling process, in which the samples were taken out of the chamber at 120°C, due to the blistering, peeling off of Al_2O_3 can be found. In comparison, another optical microscope image (Figure 3b) shows that the Al_2O_3 surface retained its integrity after utilizing the slow cooling process.

To investigate the mechanism of blister reduction, four different Al_2O_3 thin films (30 nm) were compared under various conditions: as-deposited, normal cooling process with chamber cooling to 160°C (ALD Al_2O_3-160°C), normal cooling process with chamber cooling to 120°C (ALD Al_2O_3-120°C), and slow cooling process. As can be seen from the zoom-in optical images (Figure S5, Supporting Information), the as-deposited Al_2O_3

© 2024 The Author(s). Advanced Healthcare Materials published by Wiley-VCH GmbH

21922659, 2024, 18, Downloaded from https://onlinelibrary.wiley.com/doi/10.1002/adhm.202303872 by Aalto University, Wiley Online Library on [21/07/2024]. See the Terms and Conditions (https://onlinelibrary.wiley.com/terms-and-conditions) on Wiley Online Library for rules of use; OA articles are governed by the applicable Creative Commons License

surface is quite smooth. Nevertheless, a large number of blisters can be observed on the surfaces of the samples with the normal cooling process, regardless of the sample-taking-out temperature. The optical microscope images shown in Figure S5d (Supporting Information) prove that the slow cooling process will significantly reduce the blisters. Only a few blisters can be found in this image. Image colorization and statistics (Figure S6, Supporting Information) also proves that the blisters have been reduced. P-values have been calculated between the slow-cooling sample and normal cooled samples by Coste's randomization, and the results are all 100%, which mean there is no correlation between them.

XPS measurements on various ALD Al_2O_3 thin films were then performed. The survey spectra are shown in Figure S7a–d (Supporting Information). Al_2O_3 typically exhibits a single peak at approximately 74.7 eV in the Al 2p spectrum. In the results shown here, a higher energy component appears at approximately 76.8 eV. This component can be attributed to the hydroxylation of the alumina surface. Al 2p spectra in Figure 3c show that the as-deposited Al_2O_3 has the highest OH content and the sample with slow cooling sample follows. Normal cooling processes will, however, reduce the OH content. Peak fitting (Figure 3d–g) was taken to quantify the OH ratio. A deconvolution of the O 1s peak (Figure S7e–h) also verifies this point with the values of the ratio between OH content to all O 1s and Al 2p components shown in Table S2 (Supporting Information). The ratios of OH content for the slow-cooling sample (29.5% and 13.0%) are comparable to those of the as-deposited sample (36.5% and 13.5%), which are much larger than those of the normal-cooling samples (23.5% and 7.9%; 19.3% and 2.7%).

We hypothesize that if the thin film was cooled in the ambient environment, the top and bottom surfaces of the thin film would suffer from a significant temperature difference. Thus, internal stress will result, and extra space between the Si substrate and Al_2O_3 thin film is created. This space will assist the out-gassing process, which could be a dehydration (removal of OH) process or a dehydrogenation (removal of H) process. The released H_2 or H_2O gas will generate blisters on the Al_2O_3 thin film. Thus, the normal-cooling samples with more blisters show much smaller ratios of OH contents because most of it has been released in gas form. Moreover, the decreased density of the slow-cooling sample retrieved from the X-ray reflectivity spectra shown in Figure S8 (Supporting Information) also indicates the composition change of the sample. The density values are listed in Table S3 (Supporting Information). It can be seen that the density of the Al_2O_3 slow-cooling sample shows a lower density (2.51 gcm^{-3}) than those of normal-cooling samples (3.05 and 3.04 gcm^{-3}).

2.5. Cyclic Voltammetry Characterization

At first, the microsensors were verified by cyclic voltammetry (CV) measurement in phosphate-buffered saline (PBS). Four different devices were analyzed, and the results are plotted in Figure S9 (Supporting Information). It can be seen that the four devices behaved similarly in the cyclic voltammetry characterization in the PBS solution, which confirms that the device reproducibility is acceptable.

After device verification, CV measurement was then performed. **Figure** 4a,b show 100 cycles of CV scanning in PBS solution alone and PBS solution with 10 µM of DA. It can be seen that the CV curves are quite stable in the 100 cycles (last for 8 min) except for the first few cycles. The decay in the first several cycles can be attributed to the building-up of the diffusion layer around the electrode, which will be discussed later in detail. By simple estimation of $\sqrt{2D_0t}$, the diffusion length is around 22 µm (explanation to the calculation can be seen in the Supporting Information). In the 2D oxidation current mapping in Figure 4c, the oxidation peak can be clearly identified as the dark belt around the 0.2 V position. 0.21 V was taken as the potential to extract the oxidation current evolution in the time domain, as shown in Figure 4d. The curve generally follows the exponential decay, which indicates that the oxidation current decay can be related to the analyte diffusion to the electrode surface. Figure 4e shows CV curves from the VACNF microsensor in PBS solutions with different DA concentrations (from 0.2 to 10 µM). Evident oxidation and reduction peaks can be found between 0 to 0.2 V. Zoom-in oxidation peaks are plotted in Figure 4f, and the baselines are deducted for better visibility. It is obvious that with increasing DA concentration, the oxidation current peak will increase following the trend of DA concentrations. Thus, it can be concluded that the oxidation peaks are derived from the oxidation of DA in PBS solutions.

The scan rate analysis was performed to investigate the relation between the sampling time and diffusion mechanism based on the CV measurement. The results are plotted and fitted in Figure S10 (Supporting Information). According to the Randles–Sevcik equation[57,58] and previous reports[59,60], the slope in a $log(oxidationcurrent) - log(scanrate)$ linear fitting will indicate the analyte diffusion mechanism. The details are described in the supporting text. It can be seen from Figure S10c (Supporting Information) that the slope for the first cycle measurement is 0.76, while the slope for the third one is 0.58. The first-cycle slope can be interpreted as an indicator of the adsorption-dominated charge transfer process because the most reactive sites were being taken. However, in the third cycle, the charge transfer was totally dominated by the diffusion process.

To further investigate the DA oxidation current and utilize the phenomena as the mechanism for the microsensor, oxidation currents versus DA concentrations scatters are plotted in Figure 4g. The connecting line shows two regimes, below 1 µM and over 1 µM. In the 'below 1 µM' regime, the slope is apparently steeper, while the 'above 1 µM' regime illustrates a much gentler slope. This is because, in the DA reactions, the low-concentration regime is adsorption dominated while the high-concentration regime is diffusion dominated.[61] DA molecules need to adsorb on the surface in order to react via the inner sphere route. In real applications of BoC devices, DA concentrations are usually small. The dopamine transients are on the order of 50–100 nM in rats[62] and 850 nM in monkeys.[63] Thus, the concentrations below 1 µM data points were taken for analysis to calculate the sensitivity by the calibration curve (Figure 4h). The sensitivity is calculated as in Equation (1) below:

$$S = \frac{dI}{dc} \times \frac{1}{A} \quad (1)$$

© 2024 The Author(s). Advanced Healthcare Materials published by Wiley-VCH GmbH

21922659, 2024, 18, Downloaded from https://onlinelibrary.wiley.com/doi/10.1002/adhm.202303872 by Aalto University, Wiley Online Library on [21/07/2024]. See the Terms and Conditions (https://onlinelibrary.wiley.com/terms-and-conditions) on Wiley Online Library for rules of use; OA articles are governed by the applicable Creative Commons License

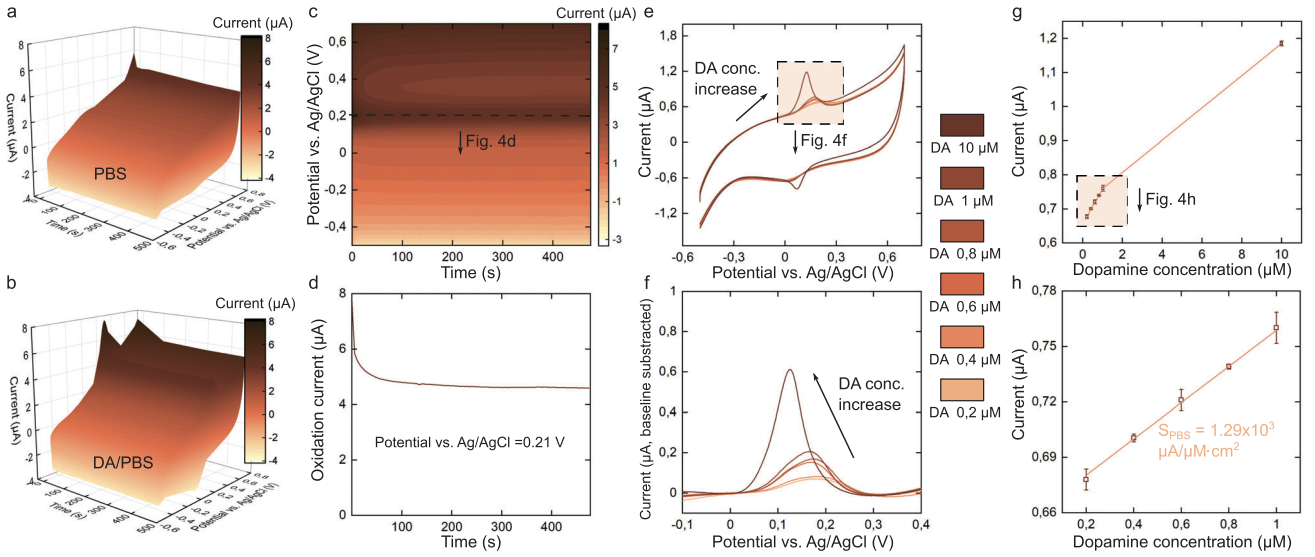

Figure 4. Cyclic voltammetry of the CNF microsensor: a) CV characterization (100 cycles) 3D plot against time in PBS solution. b) CV characterization (100 cycles) 3D plot against time in 10 μM DA solution in PBS. c) 2D mapping of the DA oxidation current versus potential and time. d) Oxidation current versus time curve based on the oxidation peak position located in sub-figure c. e) CV curves from the CNF microsensor in DA solution with different concentrations. f) Zoom-in plot of the oxidation curves. g) Oxidation current versus DA concentration plot. h) Oxidation current versus DA concentration (below 1 μM) linear fitting to calculate the sensitivity (the calibration curve).

In Equation (1), S represents the sensitivity; I is the current signal (the oxidation current in this scenario), c is the analyte concentration, while A stands for the sensing area. The dI/dc is the slope of the calibration plot shown in Figure 4h, which can be retrieved by a linear fitting. The sensing area can be extracted by the electrode diameter (100 μm). By substituting all the values into the equation, the sensitivity of our microsensor to DA in PBS solution can be retrieved, which is 1.29× 10^3μAμM^{-1}·cm^{-2}. By utilizing the 3σ method, the limit of detection (LoD) can also be calculated. The equation is as follows:

$$LoD = \frac{3\sigma_{blank}}{s} \quad (2)$$

where σ_{blank} stands for the standard deviation of the signal acquired from blank measurement. In this scenario, it is the standard deviation of the signal that the microsensor acquired in pure PBS solution, which is 1.27 nA. s represents the slope of the fitting curve in the oxidation current versus concentration plot, as shown in Figure 4h. By utilizing Equation (2), an LoD of 38 nM can be retrieved. Sensitivity and LoD acquired by other analyses will be discussed later.

Electrochemical impedance spectroscopy (EIS) is another analytical method to investigate the VACNF microsensor (Figure S11, Supporting Information). The starting part of the zoom-in spectrum (Figure S11b, Supporting Information) can be analyzed as the Rundle circuit, which includes the solution resistance and the charge transfer resistance in parallel with the double-layer capacitance. By fitting a semicircle into the Nyquist plot (Figure S11b, Supporting Information), the solution resistance and charge transfer resistance can be identified as 115 and 2.5 Ω, respectively. This fitted solution resistance is similar to the uncompensated resistance measured with the potentiostat, which verifies the EIS results. EIS in dopamine solutions with different concentrations are also performed. The results are shown in Figure S12, (Supporting Information), which indicates no significant change in both solution resistance and charge-transfer resistance. The minimal charge transfer resistance proved that the VACNF is an excellent polycrystal material for electrochemical sensors and partially explained the high sensitivity.

2.6. Control Device Analysis

As what has been stated before, one of the current state-of-the-art routes to fabricate VACNF-based microsensors is performing another photolithography process after the CNF growth to pattern the essential insulation layer. However, traditional photolithography involves many solvent procedures in the development and cleaning steps. The large surface tension in the solvent evaporation process on the VACNF-covered area will cause a 'stiction' phenomenon similar to that in MEMS fabrication.[64] Freestanding fibers will stick to each other and easily be broken in the following steps, like nitrogen drying.

In making the control device, two successive acetone and IPA rinsing steps were applied on a VACNF chip, and then gentle nitrogen drying was performed. The SEM image in **Figure 5a** shows that the device right after the fabrication process possesses a forest-like VACNF morphology. No evidence of stiction is visible. However, large numbers of broken fibers can be observed on the control device after solvent rinsing and drying (Figure 5b). It should be noted that the solvent processes in an actual photolithography routine are even more rigorous. Thus, more damage can be expected in real-life insulation layer patterning. Because of the contamination issue, we cannot perform the whole photolithography process in a cleanroom. The solvent rinsing and drying steps are used to verify the damage of the solvent to the VACNF morphology.

© 2024 The Author(s). Advanced Healthcare Materials published by Wiley-VCH GmbH

21922659, 2024, 18, Downloaded from https://onlinelibrary.wiley.com/doi/10.1002/adhm.202303872 by Aalto University, Wiley Online Library on [21/07/2024]. See the Terms and Conditions (https://onlinelibrary.wiley.com/terms-and-conditions) on Wiley Online Library for rules of use; OA articles are governed by the applicable Creative Commons License

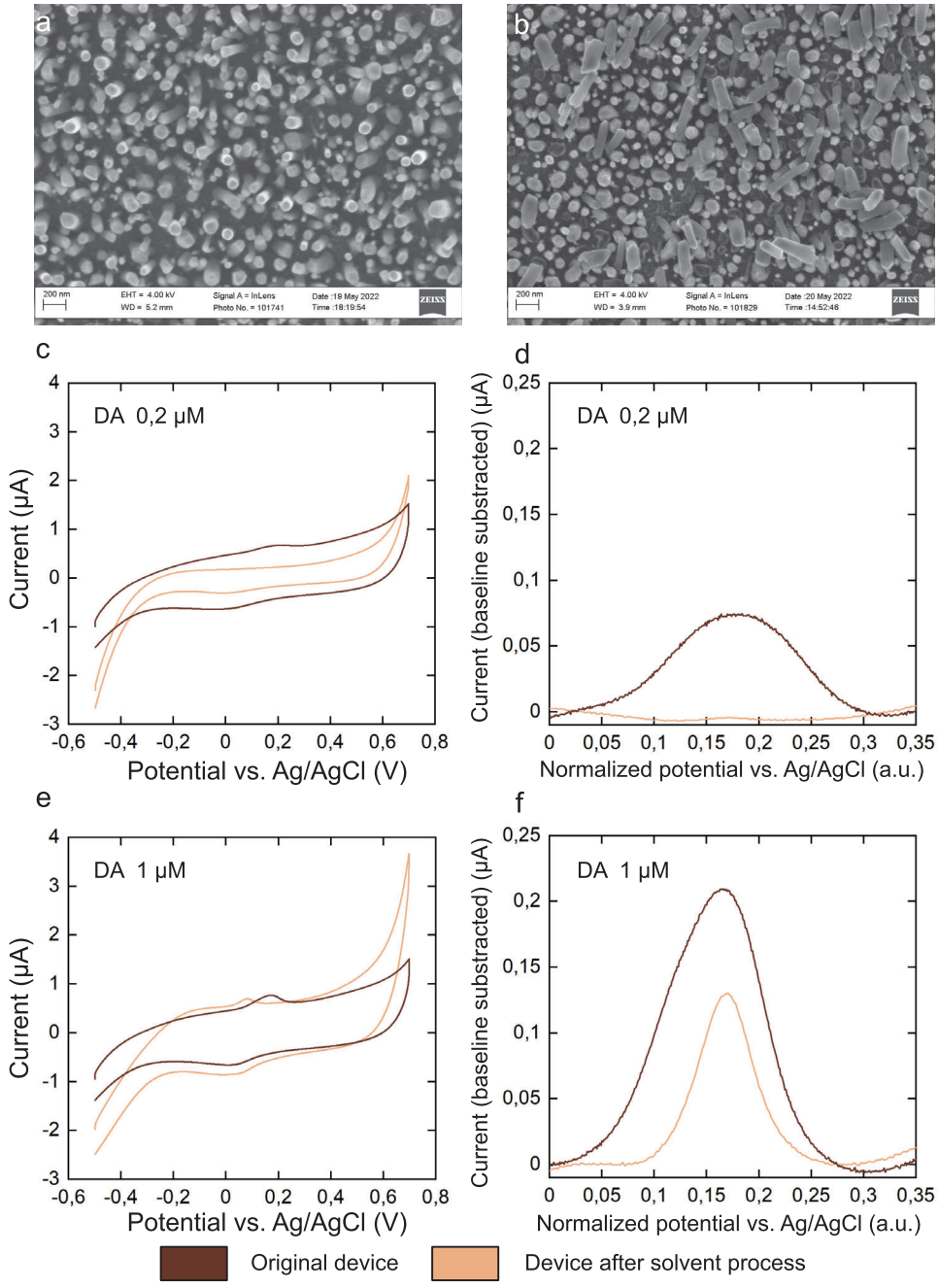

Figure 5. Control device analysis: a) SEM image of the as-deposited VACNFs. b) SEM image of the control device (VACNFs after the solvent process). c) CV curves of the original device and control device in 0.2 µ*M* of DA/PBS solution. d) CV oxidation peaks (baseline subtracted) of the original device and control device in 0.2 µ*M* of DA/PBS solution. e) CV curves of the original device and control device in 1 µ*M* of DA/PBS solution. f) CV oxidation peaks (baseline subtracted) of the original device and control device in 1 µ*M* of DA/PBS solution.

CV measurements in different concentrations of DA solutions were performed to examine the original device and the control device (Figure S13, Supporting Information). In 0.2 µM of DA solution (Figure 5c,d), the control device does not show any visible oxidation peak, while the original device shows a clear peak. In 1 µM of DA solution, both devices show oxidation peaks (Figure 5e,f). However, the peak of the original device is much larger than that of the control device. It can be concluded that the original device is more sensitive than the device after acetone and IPA rinsing and drying. This is because the original device had a large surface area due to the forest-like morphology. Because of the collapsed fibers, the control device possessed a much smaller surface area. Moreover, the most reactive adsorption sites were likely deactivated because of the collapsed fibers, reducing the oxidation current.

An important electrochemical figure-of-merit, the electron transfer rate (K_0), was calculated then. The detailed calculation process can be seen in the supporting text and Figure S14

© 2024 The Author(s). Advanced Healthcare Materials published by Wiley-VCH GmbH

21922659, 2024, 18, Downloaded from https://onlinelibrary.wiley.com/doi/10.1002/adhm.202303872 by Aalto University, Wiley Online Library on [21/07/2024]. See the Terms and Conditions (https://onlinelibrary.wiley.com/terms-and-conditions) on Wiley Online Library for rules of use; OA articles are governed by the applicable Creative Commons License

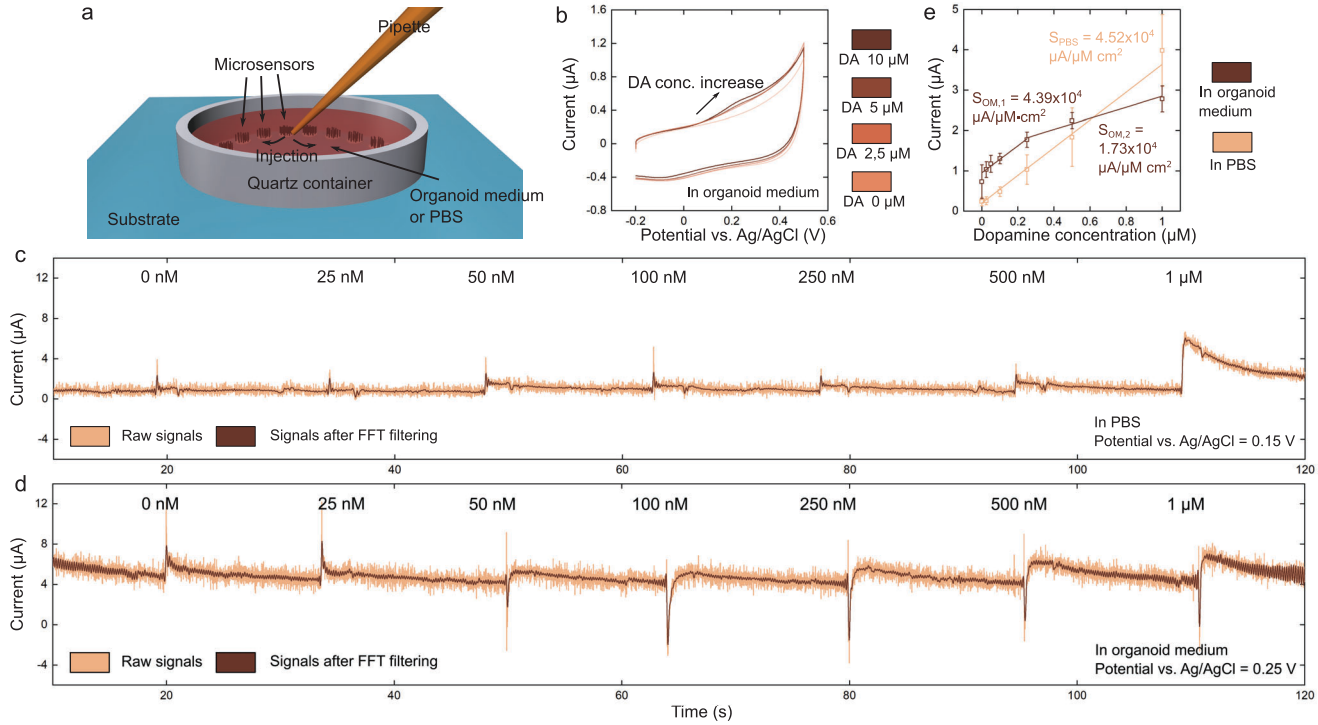

Figure 6. Chronoamperometry study of the CNF microsensor: a) Illustration of the injection process in the chronoamperometry measurement. b) CV results of DA/organoid medium solutions with different DA concentrations. c) Sample chronoamperometry curve in PBS by injections of DA solutions with different concentrations. d) Sample chronoamperometry curve in the organoid medium by injecting DA solutions with different concentrations. e. Oxidation current versus dopamine concentration scatters with linear fitting to calculate the sensitivity.

(Supporting Information). It should be noted here that it has been widely recognized by the research community that Nicholson's equation can be used to analyze the dopamine reaction on carbon fibers.[65] Interestingly, regarding the electron transfer rate, the control device (0.0775 cms^{-1}) surpasses the original device (0.0163 cms^{-1}). It is probably because the collapsed fibers promote electron transfer. It can be concluded that the large surface area of the original device and proper surface chemistry for adsorption are the keys to high performance.

Moreover, CV measurements for devices with longer CNFs have also been performed as shown in Figure S15 (Supporting Information). From Figure S15a (Supporting Information), it can be seen that the lengths of CNFs in this device is well longer than 2 μm while the aforementioned working device including CNFs ≈ 1 μm. Figure S15b,c ((Supporting Information) demonstrate that the characteristic signals are extremely hard to be recognized. By comparison shown in Figure S15d,e (Supporting Information), it can be revealed that the large background current values that makes the characteristic signals indistinguishable, which is because the larger effective surface areas of the longer CNF electrodes will increase the capacitive current.[66]

2.7. Chronoamperometry Characterization

To better understand the behavior of our VACNF microsensor, another electrochemical technique, chronoamperometry (CA), was selected to analyze the devices. Chronoamperometry is suitable for real-time neurotransmitter detection because it is fast, simple for data acquisition, easy for data processing, and it also has a higher signal-to-noise ratio.[67] Because of its unique properties, it allows us to simulate an in vitro measurement similar to that of BoC applications.

To verify its feasibility in future BoC applications, the device was measured in both PBS and an organoid medium (OM) solution, a medium solution for in vitro midbrain organoid growth.[68] The OM provides a controlled in vitro environment for cell growth and is much more complex compared to PBS solution. The base medium contains a variety of essential nutrients and proteins for the survival of the cells, and the complete organoid medium is also supplemented with a common interferent, AA. As a result, electrochemical measurement results in PBS and OM are different. The sensitivity in OM is reduced due to the fouling from proteins, etc., while the oxidation peak potential is also slightly shifted because of the presence of AA. The details of the OM recipe can be found in the Experimental section. The sensor chip setup (**Figure 6a**; Figure S16, Supporting Information) is similar to that in the CV measurement. A small volume of DA solution (10 μL) with concentrations ranging from 25 nM to 1 μM will be injected into PBS or OM in the quartz container by a pipette placed close to the electrode array to mimic the neurotransmitter release in a synapse. The injection details are described in the Experimental Section.

CV measurement was first taken to acquire the value of the oxidation peak potential as shown in Figure 6b. Then, the CA measurement was performed, in which a fixed potential

© 2024 The Author(s). Advanced Healthcare Materials published by Wiley-VCH GmbH

21922659, 2024, 18, Downloaded from https://onlinelibrary.wiley.com/doi/10.1002/adhm.202303872 by Aalto University, Wiley Online Library on [21/07/2024]. See the Terms and Conditions (https://onlinelibrary.wiley.com/terms-and-conditions) on Wiley Online Library for rules of use; OA articles are governed by the applicable Creative Commons License

Table 1. Summary of state-of-the-art devices for electrochemical DA detection.

Material	Detection (medium)	Area (μm^2)	LoD (nM)	Sensitivity ($\mu A \mu M \cdot cm^{-2}$)	Reference
CNF (microelectrode)	CV (in PBS)	7.9×10^3	38.0 ± 4.4	$(1.29 \pm 0.15) \times 10^3$	This work
	CA (in PBS)	7.9×10^3	0.243 ± 0.035	$(4.52 \pm 0.66) \times 10^4$	This work
	CA (in OM[a])	7.9×10^3	0.602 ± 0.070	$(4.39 \pm 0.51) \times 10^4$	This work
Carbon nanorods	FSCV[b] (in TBS[c])	≈ 900	60 ± 5	556 ± 445	[48]
PyC[d]	FSCV (in TBS)	500	50	900	[50]
Carbon fiber	FSCV (in TBS)	2.24×10^3	9 ± 1.8	153 ± 63	[70]
CNF (macroelectrode)	CV (in PBS)	8.1×10^7	55	0.34	[65]
Carbon cloth	DPV[e] (in PBS)	NA	180	19.2	[71]
Graphene	DPV (in PBS)	2.0×10^7	10	0.67	[72]
Au	CV (in PBS)	NA	128	0.156	[73]
Carbon sphere	CV (in PBS)	1.3×10^4	10 ± 2	≈ 331	[51]
Ag/r-GO[f] pillar	CV (in PBS)	4×10^6	5×10^{-7}	≈ 16.7	[69]
	CA (in PBS&AS[g])	4×10^6	5×10^{-7}	≈ 175	[69]
ITO[h]	CV (in PBS)	1.19×10^6	30	≈ 0.41	[74, 75]
Carbon nanograss	CV (in PBS)	1.26×10^7	NA	≈ 770	[76]

[a] OM – Organoid medium; [b] FSCV – Fast-scan cyclic voltammetry; [c] TBS – Tris buffer solution; [d] PyC – Pyrolytic carbon; [e] DPV – Differential pulse voltammetry; [f] GO – Graphene oxide; [g] AS – Artificial serum; [h] ITO – Indium tin oxide.

(oxidation peak potential) was applied on the working electrode and the current was recorded in real-time. With the DA injected and oxidized at the electrode, the oxidation current will be recorded (Figure 6c,d). Raw data were filtered by fast Fourier transform (FFT) to increase the signal-to-noise ratio and illustrate the DA oxidation current more clearly. It is clear that with a higher concentrated DA solution injected, the current pulse will become higher. It should be noted that the pipette injection involves a series of motions, which will cause disturbance of the solution. Thus, there are bumps on the curves before and after a pulse. Interpretation of these bumps is described in Figure S17 (Supporting Information).

The oxidation current values were obtained by sampling from the chronoamperometry curves and averaging from different devices. The oxidation current versus DA concentration scatters are plotted in Figure 6e. The data points from measurements in PBS show a linear relation similar to that in CV measurement. Sensitivity and LoD can be retrieved by the same methodology as in the CV results. The device shows an extremely high sensitivity of 4.52×10^4 $\mu A \mu M^{-1} \cdot cm^{-2}$, which is two-orders-of-magnitude higher than the highest state-of-the-art electrochemical DA sensor,[48,50,51,69] and the LoD is 0.243 nM. The data points in OM can be separated into two regimes, less than 0.25 µM and more than 0.25 µM. The causation should be the same as in the CV measurement (Figure 4g), adsorption. The sensitivity at low concentrations is 4.39×10^4 $\mu A \mu M^{-1} \cdot cm^{-2}$, while 1.73×10^4 $\mu A \mu M^{-1} \cdot cm^{-2}$ is the value for higher concentrations (over 0.25 µM). Here, since the targeted BoC applications are more focused on ultra-low-concentration sensing, 4.39×10^4 $\mu A \mu M^{-1} \cdot cm^{-2}$ can be considered as the sensitivity for DA detection in OM. The LoD can then be calculated as 0.602 nM, which remains at the same order of magnitude as that in the PBS solution. This phenomenon can be attributed to the sizeable white noise shown in Figure 6d brought by the mixture of molecules in the OM and also the non-permanent fouling of the surface due to surface adsorption of the medium components.

3. Discussion

Table 1 compares LoD and sensitivity between our sensor and previous milestone works. To our knowledge, the sensitivity of our VACNF microsensor is the highest in electrochemical DA detection. It is the first one that exceeds 10^4 $\mu A \mu M^{-1} \cdot cm^{-2}$. It should be noted that some electrochemical sensors (such as organic electrochemical transistor (OECT) sensors and stochastic sensors) and plasmonic sensors are not considered here because their sensitivities are not evaluated by the same criteria as the electrochemical sensors listed in Table 1. Moreover, the LoD of our VACNF microsensor is also among the highest of current state-of-the-art works.

The comparison of electrochemical DA sensors is plotted in two dimensions, LoD and sensitivity, in **Figure 7**. Here, we take our results in PBS by the CA technique. As what can be seen from this figure, nanostructured carbon microelectrodes showcase relatively large sensitivities from 31.3 to 900 because of their large surface areas, such as PyC, carbon nanorods, etc.[48,50,51,70] The sensitivity of our device is at least two-orders-of-magnitude larger than previous reports due to the extremely large surface areas brought by the dense array of nanofibers and well-reserved electrochemically active sites by our unique fabrication process.

The LoD of our device is also among the lowest. It is because our VACNF microsensors possess the highest sensitivity and integrated insulation layer, which will reduce the white noise in the electrochemical measurement. To our knowledge, in the CA measurement scheme, only the LoD of the Ag/r-GO pillar device reported by Ali et al. in 2021 (LoD = 5×10^{-7} nM)[69] is lower than ours. In the CV measurement scheme, our sensor is also

© 2024 The Author(s). Advanced Healthcare Materials published by Wiley-VCH GmbH

21922659, 2024, 18, Downloaded from https://onlinelibrary.wiley.com/doi/10.1002/adhm.202303872 by Aalto University, Wiley Online Library on [21/07/2024]. See the Terms and Conditions (https://onlinelibrary.wiley.com/terms-and-conditions) on Wiley Online Library for rules of use; OA articles are governed by the applicable Creative Commons License

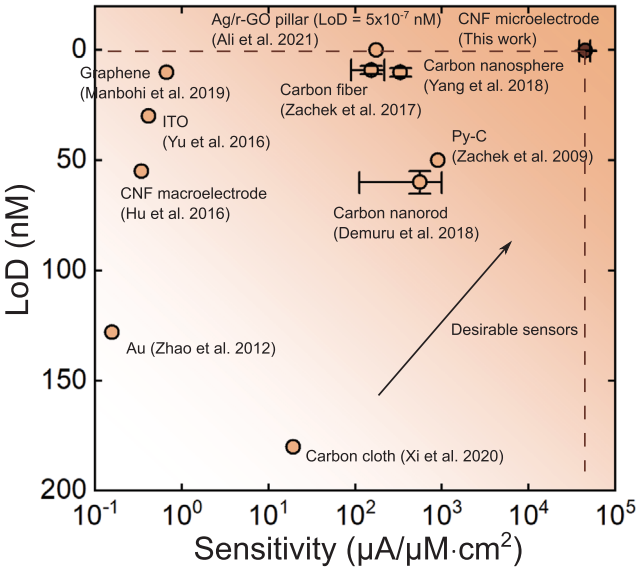

Figure 7. Comparison of our CNF microsensor with current state-of-the-art electrochemical DA sensors.

among the best along with the carbon fiber sensor,[70] carbon sphere sensor,[51] Ag/r-GO sensor,[69] and ITO sensor.[74]

4. Conclusion

In this work, we developed a unique slow-cooling technique. By integrating this technique into the microfabrication process, the favorable dense forest-like morphology of VACNFs was kept and the blisters on the Al_2O_3 insulation layer were largely reduced. VACNFs' forest-like morphology will increase electrochemical detection sensitivity, and the high-quality insulation will reduce noise in electrochemical detection. Thus, a monolithic VACNF-based microsensor to detect dopamine was successfully achieved. Because of our novel fabrication process, the device shows a record-high sensitivity of 4.52×10^4 $\mu A \mu M^{-1} \cdot cm^{-2}$ and competitive LoD of 0.243 nM in CA measurement. The superior performance will open a new window for BoC applications like the electrochemical recording of a single neuron.

5. Experimental Section

Fabrication of Dopamine Microsensors: As shown in Figure 2, the fabrication of the microsensors started from a prime silicon wafer (n-type, ⟨100⟩, resistivity: 10-20 Ωcm^{-1}, Siegert Wafer, Aachen, Germany). A Cr layer of 50 nm for wiring and pads (step (b)) was first deposited by sputtering (PlasmaLab 400, Oxford Instruments, Bristol, UK). Parameters of the sputtering can be found in Table S4 (Supporting Information). Then, to pattern the first layer of wirings and pads, an AZ 5214E photoresist (MicroChemicals GmbH., Ulm, Germany) layer was spin-coated onto the wafer by 500 rpm of spreading for 5 s and 4000 rpm of spinning for 40 s (step (c)). Afterward, the wafer was transferred onto a hotplate for soft-bake at 90°C for 2 min to evaporate solvent residues. The photoresist (PR) film would then be left at room temperature for cooling down and rehydration for 15 min. The first exposure was performed on a mask aligner (MA-6, SÜSS MicroTec, Garching, Germany), and the exposure time was 2.5 s (intensity: ≈30 $mWcm^{-2}$, 365 nm). To develop the exposed PR (step (d)), the wafer would be bathed and agitated in a mixture of AZ 351B (MicroChemicals GmbH., Ulm, Germany) and DI water (1:5, v/v). After this step, the PR pattern was formed and could be used as the etching mask. In step (e), the wafer was immersed in a bath of Cr etchant (ceric ammonium nitrate) for 10 s. After rinsing in DI water, the PR pattern was stripped in an acetone bath assisted by ultrasonication. As shown in the step (f), the bottom Cr wirings and pads were formed. Then, consecutive acetone-IPA-DI water rinses were performed on the wafer to clean the residues. After that, a 30-nm-thick Al_2O_3 film was deposited by ALD (TFS 500, Beneq, Espoo, Finland) with trimethylaluminum (TMA) and H_2O as the precursors (step (g)). The detailed parameters of the ALD deposition are shown in Table S5 (Supporting Information). Al_2O_3 film was patterned by a photolithography process identical to the previous one (step (h) and (i)). After the photolithography, the Al_2O_3 openings would be created by immersing the wafer in the mixture of AZ 351B alkaline developer and DI water (1:9, v/v) for 8 min (step (j)). Here, the AZ 351B developer acted as the etchant to Al_2O_3, and the AZ 5214E photoresist film was used as the etching mask. After the etching, the unexposed photoresist would still be kept there for future steps, and the wafer would be dried by nitrogen gas. To generate the catalyst layer for VACNF growth, 20 nm of Ni layer was then deposited onto the whole structure (step (k)) by an electron beam evaporator (IM-9912 evaporator, Instrumentti Mattila, Mynämäki, Finland). After step (k), the whole structure was placed in an acetone bath with ultrasonication to lift off the PR and unwanted Ni (step (l)). In step (m), the VACNFs were grown on the Ni film in a PECVD reactor (BlackMagic, Aixtron, Herzogenrath, Germany) at 600°C from C_2H_2 and NH_3 gases first, for which the details can be found in Table S6 (Supporting Information); the slow-cooling process was performed after the growth to keep the insulation integrated, as shown in step (n).

Material Characterization: The XPS measurements were performed with a Kratos AXIS Ultra DLD X-ray photoelectron spectrometer using a monochromated AlKα X-ray source (1486.7 eV) run at 100 W. A pass energy of 80 eV and a step size of 1.0 eV were used for the survey spectra, while a pass energy of 20 eV and a step size of 0.1 eV were used for the high-resolution spectra. Photoelectrons were collected at a 90° take-off angle under ultra-high vacuum conditions, with a base pressure typically below 1×10^{-9} Torr. The diameter of the beam spot from the X-ray was 1 mm, and the area of analysis for these measurements was 300×700 μm. All acquired spectra were charge-corrected relative to the position of graphitic bonding of carbon at 284.2 eV.

The Raman spectrum was acquired on a WITec Micro-Raman system (alpha300 RA+, WITec, Ulm, Germany). The measurement was performed in the conventional mode with laser excitation of 532 nm. The intensity of the laser was 2 W, and the objective lens used was 50×. The integration time in the data acquisition was 0.8 s.

The SEM images were obtained on a Zeiss Supra 40 system (Oberkochen, Germany). The in-lens detector was utilized, and the electron high tension (EHT) voltage was set as 4 kV.

Cyclic Voltammetry and EIS: A potentiostat (Reference 600, Gamry, Philadelphia, Pennsylvania, USA) was utilized to conduct the CV and EIS measurements. The measurement system contains three electrodes, working, reference, and counter electrodes, as shown in Figure S17 (Supporting Information). The reference electrode was a silver wire coated with AgCl, while the counter electrode was a platinum wire. A quartz ring was used to make a container on the microsensor area by attaching it with the substrate assisted by solidified PDMS. 2 mL of PBS solution was first added to the container, and the reference and counter electrode wires were dipped inside the solution. The PBS solution was prepared by mixing 8 g of NaCl, 0.2 g of KCl, 1.44 g of Na_2HPO_4, and 0.24 g of KH_2PO_4 in 800 mL of distilled water. The desired DA concentrations in the container were obtained by adding high-concentrated DA solution prepared from DA hydrochloride (Sigma–Aldrich) and the aforementioned homemade PBS solution. It should be noted that the sampling time in the CV measurements was 100 ms. No treatment before the characterization was performed.

Chronoamperometry: The chronoamperometry experiments were also performed on the Gamry Reference 600 potentiostat. The setup was similar to that in the CV and EIS measurement. An additional hotplate was added to keep the OM and PBS at 37°C.

© 2024 The Author(s). Advanced Healthcare Materials published by Wiley-VCH GmbH

21922659, 2024, 18, Downloaded from https://onlinelibrary.wiley.com/doi/10.1002/adhm.202303872 by Aalto University, Wiley Online Library on [21/07/2024]. See the Terms and Conditions (https://onlinelibrary.wiley.com/terms-and-conditions) on Wiley Online Library for rules of use; OA articles are governed by the applicable Creative Commons License

In chronoamperometric and OM cyclic voltammetry experiments, the electrolyte solution employed was either Dulbecco's Phosphate Buffered Saline (PBS, Gibco) or N2B27 culture medium, which was typically utilized for the cultivation of human midbrain organoids, provided that AA, growth factors, and dibutyryl cyclic adenosine monophosphate (dbcAMP) were included. The N2B27 medium was prepared using the previously established protocol[77] by combining DMEM/F-12 (Gibco) and Neurobasal (Gibco) at a 1:1 ratio. This medium was then fortified with N-2 supplement (17502-048, Gibco) at a dilution of 1:200, B-27 supplement (12587-010, Gibco) at a dilution of 1:100, GlutaMAX supplement (Gibco) at a ratio of 1:100, and Penicillin-Streptomycin (Gibco) at a dilution of 1:100.

Furthermore, the N2B27 medium was further enhanced to create the complete OM by the addition of specific components, including 10 $ngmL^{-1}$ of human glial cell line-derived neurotrophic factor (hGDNF, Peprotech), 10 $ngmL^{-1}$ of human brain-derived neurotrophic factor (hBDNF, Peprotech), 1 $ngmL^{-1}$ of transforming growth factor beta 3 (TGF-β3, Peprotech), 500 µM of dbcAMP (Sigma Aldrich), and 200 µM of AA (Sigma–Aldrich).

Each dopamine-containing solution was promptly prepared at the time of use using a freshly prepared dopamine stock solution, which was created by dissolving DA hydrochloride in PBS. Given the absence of 5% CO_2 in the ambient environment, the alkalinity of the cell culture medium gradually shifts. As a result, all experiments involving the culture medium were conducted within a 15-min timeframe to ensure a stable pH of 7.4.

Supporting Information

Supporting Information is available from the Wiley Online Library or from the author.

Acknowledgements

This work is financially supported by the CONNECT project, which is funded by the European Commission under Horizon 2020 program H2020-EU.1.2.2.–FET Proactive. The authors acknowledged the provision of facilities and technical support by Aalto University at Micronova Nanofabrication Centre. The authors also thank Dr. Timo Sajavaara from the Department of Physics, the University of Jyväskylä for helpful discussion and the Nanomicroscopy Center at Aalto University for their support in TEM imaging. The authors thank Dr. Hui Wang from the University of Alberta for her suggestions and discussions in graphical art design.

Conflict of Interest

The authors declare no conflict of interest.

Author Contributions

Conceptualization is performed by LM and SF. Methodology is performed by LM, and MA. Investigation is done by LM, MA, AA, YS, KM, and SS. Visualization is performed by LM. Supervision is performed by SF. Writing—original draft is completed by LM. Writing—review & editing is performed by LM, MA, KM, and SF.

Data Availability Statement

The data that support the findings of this study are available on request from the corresponding author. The data are not publicly available due to privacy or ethical restrictions.

Keywords

atomic layer deposition, brain-on-chip, carbon nanofiber, microelectrodes, neurotransmitter

Received: November 7, 2023
Revised: March 19, 2024
Published online: June 14, 2024

[1] G. D. Fischbach, *Sci. Am.* **1992**, *267*, 48.
[2] F. Crick, C. Koch, *Sci. Am.* **1995**, *273*, 84.
[3] L. Amirifar, A. Shamloo, R. Nasiri, N. R. de Barros, Z. Z. Wang, B. D. Unluturk, A. Libanori, O. Ievglevskyi, S. E. Diltemiz, S. Sances, I. Balasingham, S. K. Seidlits, N. Ashammakhi, *Biomaterials* **2022**, *285*, 121531.
[4] S. Bang, S. Jeong, N. Choi, H. N. Kim, *Biomicrofluidics* **2019**, *13*, 051301.
[5] J. G. Parker, J. D. Marshall, B. Ahanonu, Y.-W. Wu, T. H. Kim, B. F. Grewe, Y. Zhang, J. Z. Li, J. B. Ding, M. D. Ehlers, M. J. Schnitzer, *Nature* **2018**, *557*, 177.
[6] A. P. Alivisatos, A. M. Andrews, E. S. Boyden, M. Chun, G. M. Church, K. Deisseroth, J. P. Donoghue, S. E. Fraser, J. Lippincott-Schwartz, L. L. Looger, S. Masmanidis, P. L. McEuen, A. V. Nurmikko, H. Park, D. S. Peterka, C. Reid, M. L. Roukes, A. Scherer, M. Schnitzer, T. J. Sejnowski, K. L. Shepard, D. Tsao, G. Turrigiano, P. S. Weiss, C. Xu, R. Yuste, X. Zhuang, *ACS Nano* **2013**, *7*, 1850.
[7] C. Heelan, J. Lee, R. O'Shea, L. Lynch, D. M. Brandman, W. Truccolo, A. V. Nurmikko, *Commun. Biol.* **2019**, *2*, 1.
[8] M. Colombo, *J. Exp. Theor. Artif. Intell.* **2017**, *29*, 361.
[9] J. P. Lafleur, A. Jönsson, S. Senkbeil, J. P. Kutter, *Biosens. Bioelectron.* **2016**, *76*, 213.
[10] M. Baker, *Nature* **2011**, *471*, 661.
[11] M. Brofiga, P. Massobrio, *Front. Neurosci.* **2022**, *16*, 837623.
[12] B. M. Maoz, *APL Bioeng.* **2021**, *5*, 030902.
[13] M. J. Aebersold, H. Dermutz, C. Forró, S. Weydert, G. Thompson-Steckel, J. Vörös, L. Demkó, *TrAC, Trends Anal. Chem.* **2016**, *78*, 60.
[14] S. I. Ahn, Y. J. Sei, H.-J. Park, J. Kim, Y. Ryu, J. J. Choi, H.-J. Sung, T. J. MacDonald, A. I. Levey, Y. Kim, *Nat. Commun.* **2020**, *11*, 1.
[15] T.-E. Park, N. Mustafaoglu, A. Herland, R. Hasselkus, R. Mannix, E. A. FitzGerald, R. Prantil-Baun, A. Watters, O. Henry, M. Benz, H. Sanchez, H. J. McCrea, L. C. Goumnerova, H. W. Song, S. P. Palecek, E. Shusta, D. E. Ingber, *Nat. Commun.* **2019**, *10*, 1.
[16] E. Karzbrun, A. Kshirsagar, S. R. Cohen, J. H. Hanna, O. Reiner, *Nat. Phys.* **2018**, *14*, 515.
[17] J. H. Sung, Y. I. Wang, N. Narasimhan Sriram, M. Jackson, C. Long, J. J. Hickman, M. L. Shuler, *Anal. Chem.* **2018**, *91*, 330.
[18] C. Forro, D. Caron, G. N. Angotzi, V. Gallo, L. Berdondini, F. Santoro, G. Palazzolo, G. Panuccio, *Micromachines* **2021**, *12*, 124.
[19] A. Scott, K. Weir, C. Easton, W. Huynh, W. J. Moody, A. Folch, *Lab Chip* **2013**, *13*, 527.
[20] S. Imani, A. J. Bandodkar, A. Mohan, R. Kumar, S. Yu, J. Wang, P. P. Mercier, *Nat. Commun.* **2016**, *7*, 1.
[21] D. A. Soscia, D. Lam, A. C. Tooker, H. A. Enright, M. Triplett, P. Karande, S. K. Peters, A. P. Sales, E. K. Wheeler, N. O. Fischer, *Lab Chip* **2020**, *20*, 901.
[22] E. Ferrari, C. Palma, S. Vesentini, P. Occhetta, M. Rasponi, *Biosensors* **2020**, *10*, 110.
[23] M. Mir, S. Palma-Florez, A. Lagunas, M. J. López-Martínez, J. Samitier, *ACS Sens.* **2022**, *7*, 1237.
[24] M. Zamani, T. Wilhelm, A. L. Furst, *J. Electrochem. Soc.* **2022**, *169*, 047513.
[25] Z. Tavakolian-Ardakani, O. Hosu, C. Cristea, M. Mazloum-Ardakani, G. Marrazza, *Sensors* **2019**, *19*, 2037.
[26] M. Abrantes, D. Rodrigues, T. Domingues, S. S. Nemala, P. Monteiro, J. Borme, P. Alpuim, L. Jacinto, *J. Nanobiotechnology* **2022**, *20* , 495.
[27] K. E. Hubbard, A. Wells, T. S. Owens, M. Tagen, C. H. Fraga, C. F. Stewart, *Biomed. Chromatogr.* **2010**, *24*, 626.

© 2024 The Author(s). Advanced Healthcare Materials published by Wiley-VCH GmbH

21922659, 2024, 18, Downloaded from https://onlinelibrary.wiley.com/doi/10.1002/adhm.202303872 by Aalto University, Wiley Online Library on [21/07/2024]. See the Terms and Conditions (https://onlinelibrary.wiley.com/terms-and-conditions) on Wiley Online Library for rules of use; OA articles are governed by the applicable Creative Commons License

[28] J. Kim, M. Jeon, K.-J. Paeng, I. R. Paeng, *Anal. Chim. Acta* **2008**, *619*, 87.
[29] T. Yoshitake, S. Yoshitake, K. Fujino, H. Nohta, M. Yamaguchi, J. Kehr, *J. Neurosci. Methods* **2004**, *140*, 163.
[30] S. D. Niyonambaza, P. Kumar, P. Xing, J. Mathault, P. De Koninck, E. Boisselier, M. Boukadoum, A. Miled, *Appl. Sci.* **2019**, *9*, 4719.
[31] A. Vázquez-Guardado, S. Barkam, M. Peppler, A. Biswas, W. Dennis, S. Das, S. Seal, D. Chanda, *Nano Lett.* **2018**, *19*, 449.
[32] Y. Choi, J.-H. Choi, L. Liu, B.-K. Oh, S. Park, *Chem. Mater.* **2013**, *25*, 919.
[33] J. Matsui, K. Akamatsu, N. Hara, D. Miyoshi, H. Nawafune, K. Tamaki, N. Sugimoto, *Anal. Chem.* **2005**, *77*, 4282.
[34] Y. Yu, H. Y. Y. Nyein, W. Gao, A. Javey, *Adv. Mater.* **2020**, *32*, 1902083.
[35] Y. Yang, Y. Song, X. Bo, J. Min, O. S. Pak, L. Zhu, M. Wang, J. Tu, A. Kogan, H. Zhang, et al., *Nat. Biotechnol.* **2020**, *38*, 217.
[36] H.-J. Chung, M. S. Sulkin, J.-S. Kim, C. Goudeseune, H.-Y. Chao, J. W. Song, S. Y. Yang, Y.-Y. Hsu, R. Ghaffari, I. R. Efimov, et al., *Adv. Healthcare Mater.* **2014**, *3*, 59.
[37] H. Li, K. Zhou, J. Cao, Q. Wei, C.-T. Lin, S. E. Pei, L. Ma, N. Hu, Y. Guo, Z. Deng, Z. Yu, S. Zeng, W. Yang, L. Meng, *Carbon* **2021**, *171*, 16.
[38] S. Sainio, T. Palomäki, S. Rhode, M. Kauppila, O. Pitkänen, T. Selkälä, G. Toth, M. Moram, K. Kordas, J. Koskinen, T. Laurila, *Sens. Actuators B: Chem.* **2015**, *211*, 177.
[39] A. Kousar, E. Peltola, T. Laurila, *ACS Omega* **2021**, *6*, 26391.
[40] N. Isoaho, E. Peltola, S. Sainio, J. Koskinen, T. Laurila, *RSC Adv.* **2018**, *8*, 35802.
[41] J. Huang, Y. Liu, T. You, *Anal. Methods* **2010**, *2*, 202.
[42] E. Rand, A. Periyakaruppan, Z. Tanaka, D. A. Zhang, M. P. Marsh, R. J. Andrews, K. H. Lee, B. Chen, M. Meyyappan, J. E. Koehne, *Biosens. Bioelectron.* **2013**, *42*, 434.
[43] P. U. Arumugam, H. Chen, S. Siddiqui, J. A. Weinrich, A. Jejelowo, J. Li, M. Meyyappan, *Biosens. Bioelectron.* **2009**, *24*, 2818.
[44] J. E. Koehne, M. Marsh, A. Boakye, B. Douglas, I. Y. Kim, S.-Y. Chang, D.-P. Jang, K. E. Bennet, C. Kimble, R. Andrews, M. Meyyappan, K. H. Lee, *Analyst* **2011**, *136*, 1802.
[45] S. Siddiqui, P. U. Arumugam, H. Chen, J. Li, M. Meyyappan, *ACS Nano* **2010**, *4*, 955.
[46] L. Z. Swisher, L. U. Syed, A. M. Prior, F. R. Madiyar, K. R. Carlson, T. A. Nguyen, D. H. Hua, J. Li, *J. Phys. Chem. C* **2013**, *117*, 4268.
[47] T. B. Nguyen-Vu, H. Chen, A. M. Cassell, R. J. Andrews, M. Meyyappan, J. Li, *IEEE Trans. Biomed. Eng.* **2007**, *54*, 1121.
[48] S. Demuru, L. Nela, N. Marchack, S. J. Holmes, D. B. Farmer, G. S. Tulevski, Q. Lin, H. Deligianni, *ACS Sens.* **2018**, *3*, 799.
[49] M. Guillorn, T. McKnight, A. Melechko, V. Merkulov, P. Britt, D. Austin, D. Lowndes, M. Simpson, *J. Appl. Phys.* **2002**, *91*, 3824.
[50] M. K. Zachek, P. Takmakov, B. Moody, R. M. Wightman, G. S. McCarty, *Anal. Chem.* **2009**, *81*, 6258.
[51] C. Yang, Q. Cao, P. Puthongkham, S. T. Lee, M. Ganesana, N. V. Lavrik, B. J. Venton, *Angew. Chem., Int. Ed.* **2018**, *57*, 14255.
[52] A. C. Ferrari, J. C. Meyer, V. Scardaci, C. Casiraghi, M. Lazzeri, F. Mauri, S. Piscanec, D. Jiang, K. S. Novoselov, S. Roth, A. K. Geim, *Phys. Rev. Lett.* **2006**, *97*, 187401.
[53] K. Sinha, L. Meng, Q. Xu, X. Wang, *Mater. Lett.* **2021**, *286*, 129268.
[54] M. C. Biesinger, B. P. Payne, A. P. Grosvenor, L. W. Lau, A. R. Gerson, R. S. C. Smart, *Appl. Surf. Sci.* **2011**, *257*, 2717.
[55] R. Matsumura, N. Fukata, *ACS Appl. Mater. Interfaces* **2021**, *14*, 1472.
[56] M. Broas, H. Jiang, A. Graff, T. Sajavaara, V. Vuorinen, M. Paulasto-Kröckel, *Appl. Phys. Lett.* **2017**, *111*, 141606.
[57] P. Nayak, N. Kurra, C. Xia, H. N. Alshareef, *Adv. Electron. Mater.* **2016**, *2*, 1600185.
[58] P. Zanello, C. Nervi, F. F. De Biani, *Inorganic electrochemistry: theory, practice and application*, Royal Society of Chemistry, London **2019**.
[59] K. Li, X. Wang, S. Li, P. Urbankowski, J. Li, Y. Xu, Y. Gogotsi, *Small* **2020**, *16*, 1906851.
[60] M. Ghidiu, M. R. Lukatskaya, M.-Q. Zhao, Y. Gogotsi, M. W. Barsoum, *Nature* **2014**, *516*, 78.
[61] B. D. Bath, D. J. Michael, B. J. Trafton, J. D. Joseph, P. L. Runnels, R. M. Wightman, *Anal. Chem.* **2000**, *72*, 5994.
[62] D. L. Robinson, A. Hermans, A. T. Seipel, R. M. Wightman, *Chem. Rev.* **2008**, *108*, 2554.
[63] E. W. Schluter, A. R. Mitz, J. F. Cheer, B. B. Averbeck, *PloS One* **2014**, *9*, e98692.
[64] Z. Yapu, *Acta Mech. Sin.* **2003**, *19*, 1.
[65] L. Hu, X. Peng, K. Huo, R. Chen, J. Fu, Y. Li, L. Y. S. Lee, K.-Y. Wong, P. K. Chu, *ACS Appl. Mater. Interfaces* **2016**, *8*, 28872.
[66] C.-y. Liu, A. J. Bard, F. Wudl, I. Weitz, J. R. Heath, *Electrochem. Solid-State Lett.* **1999**, *2*, 577.
[67] H. Jo, J. Her, H. Lee, Y.-B. Shim, C. Ban, *Talanta* **2017**, *165*, 442.
[68] L. M. Smits, L. Reinhardt, P. Reinhardt, M. Glatza, A. S. Monzel, N. Stanslowsky, M. D. Rosato-Siri, A. Zanon, P. M. Antony, J. Bellmann, S. M. Nicklas, K. Hemmer, X. Qing, E. Berger, N. Kalmbach, M. Ehrlich, S. Bolognin, A. A. Hicks, F. Wegner, J. L. Sterneckert, J. C. Schwamborn, *NPJ Parkinson's Disease* **2019**, *5*, 1.
[69] M. Ali, C. Hu, B. Yuan, S. Jahan, M. S. Saleh, Z. Guo, A. J. Gellman, R. Panat, *Nat. Commun.* **2021**, *12*, 1.
[70] S. Demuru, H. Deligianni, *J. Electrochem. Soc.* **2017**, *164*, G129.
[71] X. Xi, D. Wu, W. Ji, S. Zhang, W. Tang, Y. Su, X. Guo, R. Liu, *Adv. Funct. Mater.* **2020**, *30*, 1905361.
[72] A. Manbohi, S. H. Ahmadi, *Sens. Bio-Sens. Res.* **2019**, *23*, 100270.
[73] Y. Zhao, S.-H. Li, J. Chu, Y.-P. Chen, W.-W. Li, H.-Q. Yu, G. Liu, Y.-C. Tian, Y. Xiong, *Biosens. Bioelectron.* **2012**, *35*, 115.
[74] Y. Yu, M. H. Shamsi, D. L. Krastev, M. D. Dryden, Y. Leung, A. R. Wheeler, *Lab Chip* **2016**, *16*, 543.
[75] Y. Yu, R. P. de Campos, S. Hong, D. L. Krastev, S. Sadanand, Y. Leung, A. R. Wheeler, *Microsyst. Nanoeng.* **2019**, *5*, 1.
[76] A. Asif, A. Heiskanen, J. Emnéus, S. S. Keller, *Electrochim. Acta* **2021**, *379*, 138122.
[77] J. Jarazo, K. Barmpa, J. Modamio, C. Saraiva, S. Sabaté-Soler, I. Rosety, A. Griesbeck, F. Skwirblies, G. Zaffaroni, L. M. Smits, J. Su, J. Arias-Fuenzalida, J. Walter, G. Gomez-Giro, A. S. Monzel, X. Qing, A. Vitali, G. Cruciani, I. Boussaad, F. Brunelli, C. Jäger, A. Rakovic, W. Li, L. Yuan, E. Berger, G. Arena, S. Bolognin, R. Schmidt, C. Schröder, P. M. A. Antony, et al., *Movement Disorders* **2022**, *37*, 80.

© 2024 The Author(s). Advanced Healthcare Materials published by Wiley-VCH GmbH

21922659, 2024, 18, Downloaded from https://onlinelibrary.wiley.com/doi/10.1002/adhm.202303872 by Aalto University, Wiley Online Library on [21/07/2024]. See the Terms and Conditions (https://onlinelibrary.wiley.com/terms-and-conditions) on Wiley Online Library for rules of use; OA articles are governed by the applicable Creative Commons License